TOPOGRAPHIC SUPPORT IN ICY SHELLS OF OCEAN WORLDS: INVESTIGATING WAVELENGTH DEPENDENCE OF AIRY ISOSTASY. W. S. Tucker[1] and A. J. Dombard[1], [1]Dept. of Earth and Environmental Sciences, University of Illinois Chicago, 845 W. Taylor St., 2440 SES, Chicago, IL 60607 (wtucke5@uic.edu).

Introduction: Understanding how topography is supported on planetary bodies can provide information on the thermal and structural histories of their interiors. This concept is especially important for icy, ocean-world satellites, whose global sub-surface ocean may provide an environment to foster life [1]. On terrestrial bodies, topography is generally supported by some combination of lithospheric strength and lateral variations in either crustal thickness (Airy isostasy) or density (Pratt isostasy). At the shortest wavelengths, the strength of the lithosphere is able to support fully the topographic load. At sufficiently long wavelengths, the rigidity of the lithosphere is reduced, and the topography is compensated by isostasy.

The concept of surface topography being compensated by an opposing topography at the base of the ice shell (i.e., Airy isostasy) has been adopted to constrain the shell and internal structure of icy satellites in our outer solar system. Estimates of Europa's minimum shell thickness have been determined from abundant short wavelength topographic features [e.g., 2-4]. Furthermore, geophysical models of intermediate wavelength features on icy satellites have been unable to remain buoyantly supported over timescales relative to the age of the surface [e.g., 5, 6].

Airy isostasy is an enticing assumption to make when considering the nature of ice shells due to its simplicity: it allows gravity and topography data, collected by spacecraft, to be interpreted while only needing to constrain density. It is still unclear, though, when its use is appropriate based on observations from gravity and topographic data of icy satellites. By definition, the material near the base of the ice shell is approaching its melting point, and it should therefore be weak over geologic time scales. In principle, this limits the shell's ability to transfer buoyancy stress to support surface topography. Here, we examine the stability of buoyantly supported topography over geologic time scales from local to global spatial scales.

Methods: We use the commercially available MSC.Marc finite element package to test systematically buoyant support of topography in icy shells. The software is well vetted for investigations into the lithospheres of icy satellites [e.g., 7, 8]. Though applicable to all icy-ocean worlds, we use Europa to constrain the parameters of our simulations. We utilize planar half space meshes for wavelengths starting at 10 km, increasing logarithmically up to a hemispheric wavelength scale (i.e., spherical harmonic degree 2). The meshes are split into an outer ice shell, ostensibly 20 km thick [9], with a density of 920 kg m^{-3}, and an underlying ocean with a density of 1000 kg m^{-3} (Fig. 1). Sinusoidal surface topography is generated with an amplitude h of 100 m, and the corresponding topographic root is created assuming an initial state of isostatic equilibrium.

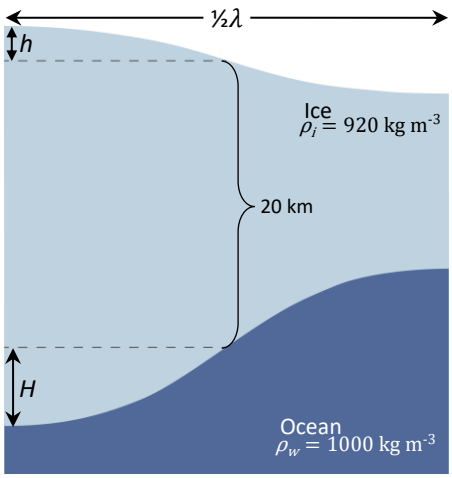

Figure 1. Schematic of initial model set up. Surface topography has an amplitude h of 100 m. The amplitude of the topographic root H with the indicated density contrast is 1150 m.

We run steady state thermal simulations locking the surface temperature T_s to 100 K, and the temperature at the base of the ice shell T_b to the melting point of ice, 273 K ($q \approx 28$ mW m^{-3}). Heat flows on Europa could be higher, resulting in a convective base of the shell; however for our purposes, the situation is mechanically identical: a structurally weak base overlain by a (thinner) lithosphere. The results of the thermal simulation are then transferred into the mechanical simulation. For water ice, we use material and rheological properties from laboratory measurements [10, 11]. The water underneath the ice shell does not provide resistance due to its lack of material strength. Rather, it provides a buoyant restoring force. The viscosity is so low compared to the viscosity of the lithospheric ice that it just needs to accommodate space for the deforming ice as fast as the ice is deforming. Therefore, we set the material properties of water to be the same as the ice layer, with the exception of the density contrast.

To test buoyant support, we run three variations for each wavelength: (1) with the aforementioned parameters, and (2) with the density contrast removed (i.e., no buoyancy, thus precluding isostasy), and (3) with a flat ice-ocean interface, thereby removing the assumption of an initial state of isostatic equilibrium.

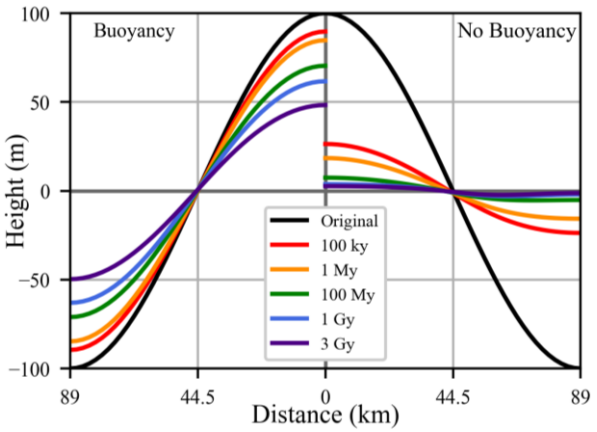

Figure 2. Example finite element simulation of the evolution of surface topography with a wavelength of 178 km for simulations with an ice-above-ocean mesh (left side of x-axis) and an all-ice mesh (right side of x-axis).

Results: At short wavelengths (less than ~30 km), topography on the surface is stable over geologic times. The initial root topography, though, relaxes by ~95% of its original size. For intermediate wavelengths (~100-600 km), the surface and root topography both relax to just over half of their original amplitudes. The loss of topography is much greater in simulations of the "all-ice" meshes that lack buoyancy (e.g., Fig. 2). This loss of topography in the non-buoyant simulations accelerates as the wavelength increases. Furthermore, the loss of root topography is not in equilibrium with the loss of the surface topography (Fig. 3): when comparing the simulated root to one in isostatic equilibrium with the surface topography, the simulated root relaxes faster and loses more topography at short wavelengths. That trend reverses for intermediate wavelengths. At long wavelengths (greater than 1000 km), the surface and root topography are stable over the time period of the simulations. However, this topography is only stable with a root that is initially in isostatic equilibrium.

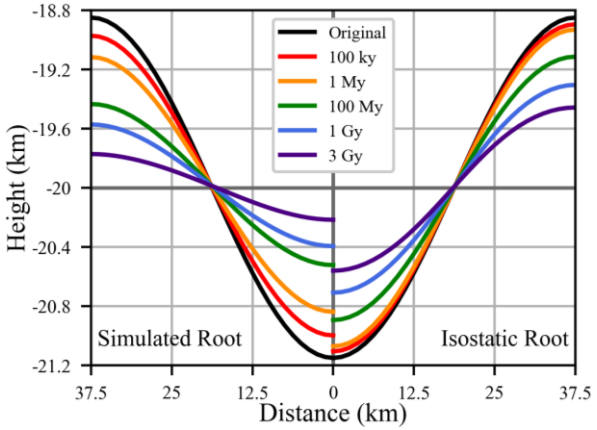

Figure 3. Evolution of the simulated root topography for a 75 km wavelength (left side of x-axis) and the topography for a root that was in isostatic equilibrium with the simulated surface topography (right side of x-axis).

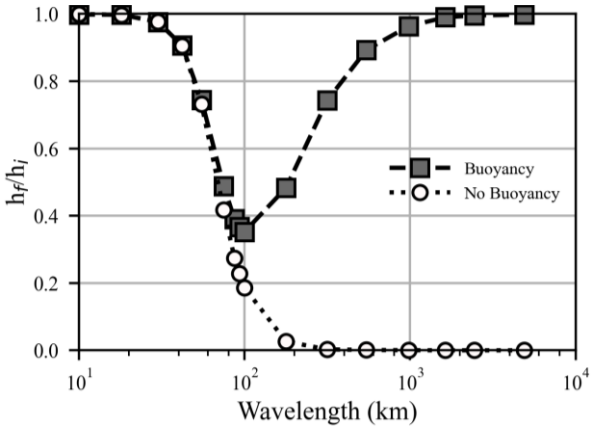

Figure 4. Ratio of the final amplitude of the surface topography h_f to the initial amplitude h_i for the simulations with buoyancy and without buoyancy.

Discussion: Application of Airy isostasy to icy shells is more complex than for terrestrial worlds. Figure 4 shows the ratio of final to initial topographic amplitudes at the surface, for the case of assumed initial isostasy. Because of an isostatically balanced start, this ratio should stay at 1 if the precepts of Airy isostasy hold. The lithosphere begins to lose its ability to support the surface load at wavelengths between 30 and 40 km, where h_f/h_i for both the buoyant and non-buoyant simulations begin to decrease, but buoyancy begins to provide support for wavelengths larger than ~100 km.

The concept can be visualized using a seat cushion analogy. If a finger pressed in, stresses are diffused in the foam, and the opposite side is negligibly deformed. Similarly, at short wavelengths where the lithosphere supports the surface topography, the base of the ice shell simply relaxes away. If someone sits on a seat cushion, though, that wider load would need to diffuse over a much deeper distance than the thickness of the cushion, so some weight is transferred to the base of the cushion. This scenario is the case for the base of the ice-shell, where the longer wavelength topography remains at the base of the ice shell. Unlike the short wavelength case, the basal topography will not relax away, because the narrow vertical flow region relative to the required lateral distance results in a highly channelized lateral flow.

References: [1] Marion, G. M., et al. (2003) *Astrobiology*, 3(4). [2] Michaut, C. & Manga, M. (2014) *JGR-Planet*, 119(3). [3] Pappalardo, R. T. et al. (1998) *Nature*, 391(6665) [4] Singer K. N. et al. (2021) *Icarus* 364(114465). [5] Kay J. P. et al. (2018) LPS XLIX, Abstract #2212. [6] Schurmeier L. R. et al. (2016) LPS XLVII, Abstract #2197. [7] Dombard, A.J. & McKinnon, W.B. (2006) *JGR*, 111, E01001. [8] Damptz, A.L. & Dombard, A.J. (2011) *Icarus*, 216. [9] Hussmann H. et al. (2002) *Icarus*, 156. [10] Gammon, L. S. et al. (1980) *J Glaciol*, 25(91). [11] Goldsby, D. L. & Kohlstedt D. L. (2001) *JGR-Sol Ea*, 106(B6).